SPATIAL GENETICS

Embryo-scale, single-cell spatial transcriptomics

Sanjay R. Srivatsan[1]†, Mary C. Regier[2,3]†, Eliza Barkan[1,4], Jennifer M. Franks[1], Jonathan S. Packer[5], Parker Grosjean[2], Madeleine Duran[1], Sarah Saxton[2], Jon J Ladd[6], Malte Spielmann[7,8], Carlos Lois[9], Paul D. Lampe[6], Jay Shendure[1,10,11,12]*, Kelly R. Stevens[2,3,12,13]*, Cole Trapnell[1,10,12]*

Spatial patterns of gene expression manifest at scales ranging from local (e.g., cell-cell interactions) to global (e.g., body axis patterning). However, current spatial transcriptomics methods either average local contexts or are restricted to limited fields of view. Here, we introduce sci-Space, which retains single-cell resolution while resolving spatial heterogeneity at larger scales. Applying sci-Space to developing mouse embryos, we captured approximate spatial coordinates and whole transcriptomes of about 120,000 nuclei. We identify thousands of genes exhibiting anatomically patterned expression, leverage spatial information to annotate cellular subtypes, show that cell types vary substantially in their extent of spatial patterning, and reveal correlations between pseudotime and the migratory patterns of differentiating neurons. Looking forward, we anticipate that sci-Space will facilitate the construction of spatially resolved single-cell atlases of mammalian development.

Single-cell methods have the potential to transform our understanding of organismal development. In diverse models of embryogenesis, we and others have performed “whole-organism” profiling of gene expression or chromatin accessibility at single-cell resolution (*1*–*7*), yielding a richer view of the emergence and trajectories of cell types than was previously available or possible (*8*, *9*).

Cells’ spatial organization plays a central role in normal development and homeostasis, as well as in pathophysiology. However, a key limitation of most single-cell molecular profiling methods is that they operate on disaggregated cells or nuclei. Although in situ methods can measure the expression of many or all genes while retaining spatial information (*10*), these methods also have limitations (fig. S1). Some, including the original “spatial transcriptomics” (*11*) and Slide-seq (*12*) methods, barcode and then count mRNAs derived from positions across patterned arrays. Although these methods can be implemented at a range of spatial scales, the boundaries of spots have no natural correspondence to the boundaries of cells. Therefore, they yield aggregate profiles of small regions encompassing multiple cells and/or portions of cells rather than truly resolving individual cells. Other methods, including MERFISH (*13*), seqFISH (*14*), and FISSEQ (*15*), rely on in situ hybridization or sequencing to measure the expression of many genes while retaining single-cell (or even subcellular) resolution within each field of view. However, such methods are typically limited by long image acquisition times and complex instrumentation requirements. In sum, existing techniques necessitate tradeoffs such that assaying the whole transcriptomes of individual cells over large territories remains impractical.

Spatial labeling of nuclei with hashing oligonucleotide

Previously, we developed sci-Plex, a method for labeling or “hashing” nuclei using unmodified DNA oligos before single-cell RNA sequencing with combinatorial indexing (sci-RNA-seq) (*16*). To leverage this workflow to capture spatial information, we spatially arrayed unique combinations of hashing oligos, and then transferred these oligos to nuclei within a tissue slice by diffusion (*17*). These hashing oligos, recovered in association with sci-RNA-seq profiles, capture each cell’s approximate tissue coordinates upon sequencing.

As a proof of concept of this “sci-Space” approach, hashing oligos were spotted onto glass slides coated with dried agarose. These grids contained 7056 uniquely barcoded spots spanning a 18 mm by 18 mm area (mean radius of 73.2 ± 14.1 μm; mean spot-to-spot center distance of 222 ± 7.5 μm; fig. S2). About 5% of spots, constituting an identifiable pattern, were also loaded with SYBR green fluorescent dye. After transferring the oligos to the tissue, the grid could be registered with an image of the tissue using these concurrently imaged fluorescent fiduciaries (figs. S2 and S3). After optimization of hashing oligo concentrations and dissociation protocols (figs. S4 and S5), our protocol comprised four steps: (i) fresh-frozen tissue is sectioned; (ii) sectioned tissue is permeabilized with a solution containing a slide-specific oligo and physically juxtaposed to a glass slide bearing the spatially gridded hashing oligos; (iii) during oligo transfer, the assembly is imaged; and (iv) nuclei from the tissue on the slide are extracted, fixed, and subjected to sci-RNA-seq (Fig. 1A and figs. S6 and S7).

Spatially resolved single-cell sequencing of the mouse embryo

We applied sci-Space to profile 14 sagittal sections derived from two embryonic day 14 (E14.0) mouse embryos (C57BL/6N). After sequencing, quality filtering (*18*), and assignment of each cell to a slide (on the basis of its slide-specific hashing oligo), our dataset comprised 121,909 spatially resolved single-cell transcriptomes [mean 2514 unique molecular identifiers (UMIs) and mean 1231 genes detected per cell], without apparent batch effects between slides or embryos (figs. S8 and S9). This corresponds to capture of 164 nuclei/mm^2 of tissue on average, or sampling of 2.2% of the estimated nuclei present (fig. S10). Rather than annotating cell types ab initio, we co-embedded (*19*, *20*) these data with a published, nonspatial sci-RNA-seq mouse organogenesis cell atlas dataset spanning E9.5 to E13.5 (*1*) and cells from a developing mouse brain atlas (DMBA) spanning E13.5 to E14.5 (*21*). Reassuringly, these E14.0 data integrated well with both datasets (Figs. 1B and fig. S11). Draft cell type annotations, inferred by nearest-neighbor label transfer, were highly concordant with those recovered by Garnett (*22*), a semisupervised annotation algorithm (fig. S11). These annotations were then refined by manual inspection of differentially expressed genes (Fig. 1C and data file S1).

Images of sectioned embryos and sequencing data were co-registered using SYBR waypoints (*23*, *24*) (Fig. 2A and figs. S12 and S13). Each nucleus was mapped to the position matching its highest combination of spot and sector oligos within the imaged section. For ~9% of nuclei, the top assignment was not located near any other nuclei of the same cell type; for such “outliers,” alternative mappings were considered. Altogether, nuclei were well localized (fig. S8, C to F) to one of 15,102 spatial positions across 14 sections; on average, each spatial position was assigned 8.1 nuclei (10.5 SD) (fig. S14). To quantify the anatomical distribution of cell type annotations, each section was segmented by organ (Fig. 2B and fig. S15), aided by immunostaining of adjacent sections (*25*) (fig. S16). Neurons mapped largely within the

---

[1]Department of Genome Sciences, University of Washington, Seattle, WA, USA. [2]Department of Bioengineering. University of Washington, Seattle, WA, USA. [3]Institute for Stem Cell and Regenerative Medicine, Seattle, WA, USA. [4]Molecular and Cellular Biology Program, University of Washington, Seattle, WA, USA. [5]Foresite Labs, Boston, MA, USA. [6]Translational Research Program, Public Health Sciences, Fred Hutchinson Cancer Research Center, Seattle, WA, USA. [7]Institute of Human Genetics, University of Lübeck, Lübeck, Germany. [8]Human Molecular Genomics Group, Max Planck Institute for Molecular Genetics, Berlin, Germany. [9]Division of Biology and Biological Engineering, California Institute of Technology, Pasadena, CA, USA. [10]Allen Discovery Center for Cell Lineage Tracing, Seattle, WA, USA. [11]Howard Hughes Medical Institute, University of Washington, Seattle, WA, USA. [12]Brotman Baty Institute for Precision Medicine, Seattle, WA, USA. [13]Department of Laboratory Medicine and Pathology, Seattle, WA, USA.
***Corresponding author. Email: shendure@uw.edu (J.S.); ksteve@uw.edu (K.R.S.); coletrap@uw.edu (C.T.)**
†These authors contributed equally to this work.

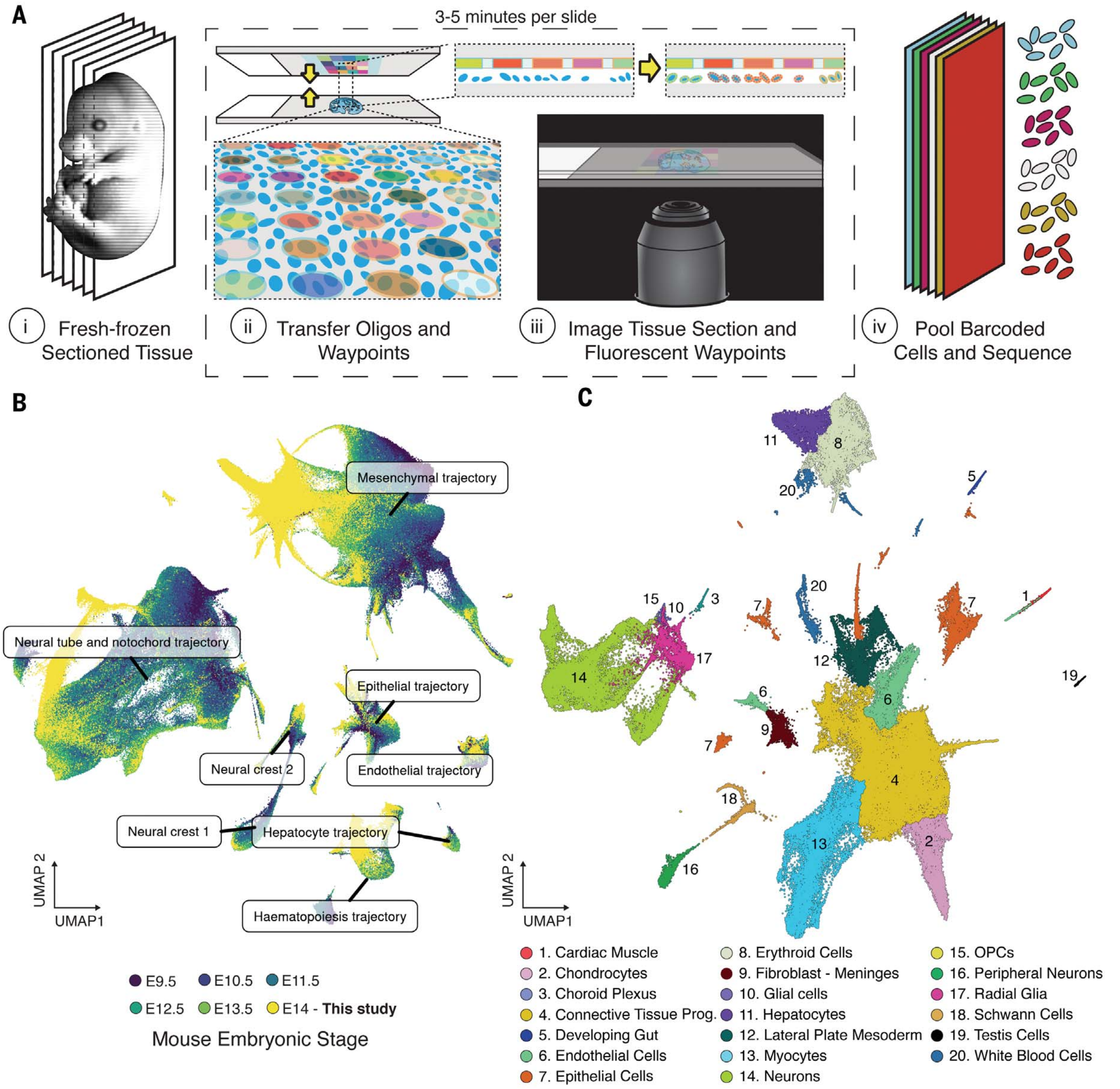

Fig. 1. sci-Space recovers single-cell transcriptomes while recording spatial coordinates. (**A**) Arrayed single-stranded oligos were transferred onto permeabilized nuclei in fresh-frozen tissue sections and imaged. Cells from each slide were also labeled with a section-identifying barcode so that multiple sections could be pooled before sci-RNA-seq. (**B**) Joint embedding of E14.0 single-cell transcriptomes from this study and published data spanning E9.5 to E13.5 (*1*). Major trajectories are labeled. (**C**) UMAP embedding of 121,909 cells from sectioned E14.0 mouse embryos. Cell types are denoted by color and number in legend.

spinal cord and brain outlined by cells of the developing meninges, cardiomyocytes within the heart, and white blood cells throughout the organism (Fig. 2, C and D, and figs. S18 and S17). Analysis with Giotto (*26*), an unsupervised tool for segmenting spatial transcriptomic images into tissue "domains" of similar cell type composition, revealed 22 domains shared across sci-Space slides. In addition to detecting boundaries between major organs, Giotto was able to automatically recognize more complex domains with distributions extending throughout the embryo (e.g., mesenchymal tissue and cartilage) (fig. S19).

Finally, wherever cells are captured, sci-Space data enable the visualization of any gene in the transcriptome akin to an in situ hybridization, albeit at lower spatial resolution. For example, a sci-Space "digital in situ" of the dopamine transporter *Slc6a3* highlights a cluster of dopaminergic neurons at the midbrain-hindbrain boundary, consistent with stage- and section-matched whole-mount in situ data (*27*) (Fig. 2E and fig. S20). Unlike conventional in situ data, sci-Space data also resolve gene expression by cell type. For example, in the heart, both cardiomyocytes and endothelial cells express the growth factor *Fgf1*, whereas only cardiomyocytes express the growth factor receptors *Fgfr1*, *Fgfr2*, and *Fgfr3* (Fig. 2F).

Contrasting sci-Space and spatial transcriptome capture (STC) methods

A key distinction between sci-Space and STC methods (fig. S1, left) is that because STC methods capture transcripts from lysed tissue sections (*11*, *12*), each spot can include RNA from multiple cells and/or portions of cells. As such, STC methods are limited in their ability to resolve gene expression variation within individual cells or cell types. To quantify the consequences of this limitation, we spatially aggregated

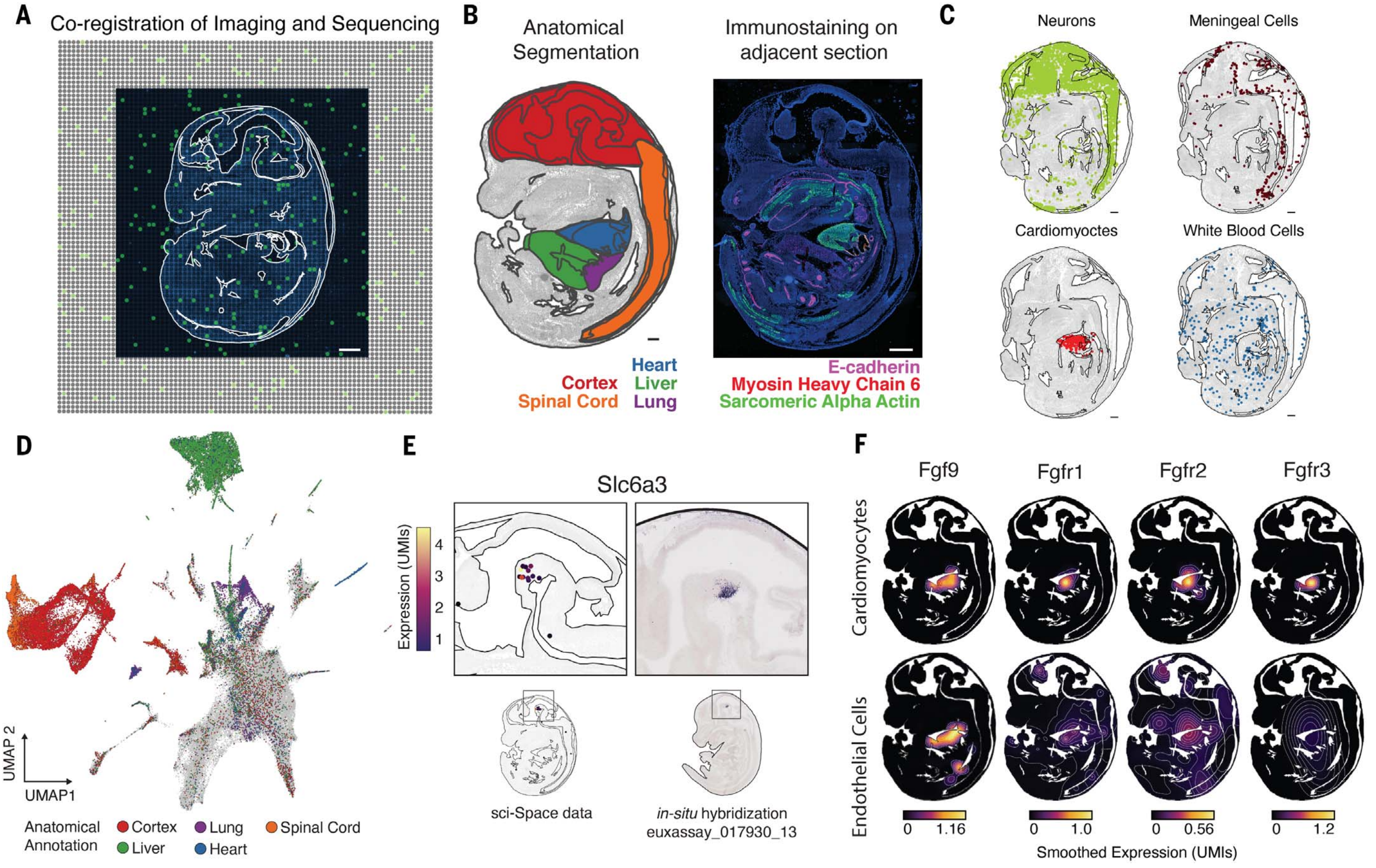

Fig. 2. sci-Space captures spatially and cell-type–resolved gene expression across the embryo. (**A**) Co-registered 4′,6-diamidino-2-phenylindole (DAPI)–stained section image and oligo array superimposed. SYBR waypoints are highlighted in green. (**B**) Anatomical regions of slide 1 (left) and an adjacent immunostained serial section aligned to slide 1 (right). (**C**) Highlighted cell types mapping to a single slide. (**D**) UMAP embedding colored by anatomical regions. (**E**) Gene expression of dopamine transporter *Slc6a3* from sci-Space data (left) and published (*27*) section/stage matched in situ (right). (**F**) Smoothed percentage of gene expression for *Fgf1*, *Fgfr1*, *Fgfr2*, and *Fgfr3* in cardiomyocytes (top) or endothelial cells (bottom). Color is scaled to maximum percentage within each gene. Scale bars in (A) to (C), 0.5 mm.

transcriptomes from sci-Space nuclei, effectively creating a “mock-STC" dataset. Cell types and clusters readily discernible in the single-cell data were challenging to resolve in the mock-STC data (fig. S21, A to C). One approach to ameliorating this limitation involves mapping cells profiled by nonspatial single-cell RNA-seq onto a STC “scaffold”, thereby imputing cellular locations within a tissue (*20*, *28*). To assess the viability of this approach, we applied such imputation to mock STC data and compared it with the single-nucleus data used to derive it (fig. S21, D and E). The mean distance between a nucleus' imputed position and its measured position was 11.6 spots (~2.5 mm), a measure that varied by cell type (fig. S21F). Thus, despite sampling fewer transcripts than STC methods (fig. S21, G to I), sci-Space's single-cell resolution—that is, its ability to unambiguously ascertain sets of transcripts expressed in the same cell—represents a key advantage over STC methods.

Analogously, we posited that sci-Space data could serve as a scaffold for the imputation of locations of cells profiled by nonspatial single-cell RNA-seq but with the advantage of matching single-cell transcriptomes. To test this, we aligned neurons from sci-Space and the DMBA. Transfer of dissection-based DMBA anatomic annotations were consistent with sci-Space coordinates (fig. S23). Furthermore, this alignment mapped hundreds of DMBA transcriptional clusters to specific positions, many spatially restricted (fig. S23). For example, of 193 transcriptomic clusters from La Manno et al. (*21*) that mapped to slides 13 and 14, 94 and 115 clusters displayed statistically significant focal enrichment, respectively [false discovery rate (FDR) < 0.01; Getis-Ord Local G].

Spatial patterns of gene expression across cell types

To systematically examine these data for spatially patterned, cell-type–specific gene expression across the E14.0 embryo, we quantified spatial autocorrelation, the degree to which the cells expressing a given gene are spatially proximate. Testing each annotated cell type separately, we identified hundreds to thousands of genes exhibiting positive spatial autocorrelation per cell type (see the supplementary materials, file S2; Moran's test, FDR < 0.001). Among the cell types analyzed, connective tissue progenitors and neurons had the most spatially autocorrelated genes detected (Fig. 3A; mean 12,150 ± 2270 and 8623 ± 3846 genes per slide, respectively).

One explanation for such spatial autocorrelation of genes within a cell type would be the presence of spatially restricted, unannotated cell subtypes. For example, upon subclustering of connective tissue progenitors, we can indeed find spatially restricted cell subtypes (fig. S24, A and B), such that the genes defining these subtypes are expected to be spatially autocorrelated. Alternatively, a gene's spatial pattern of expression could arise from spatially restricted gene expression contributed by multiple cell subtypes. To distinguish between these scenarios, we calculated each gene's spatial autocorrelation (spatial Moran's I) and

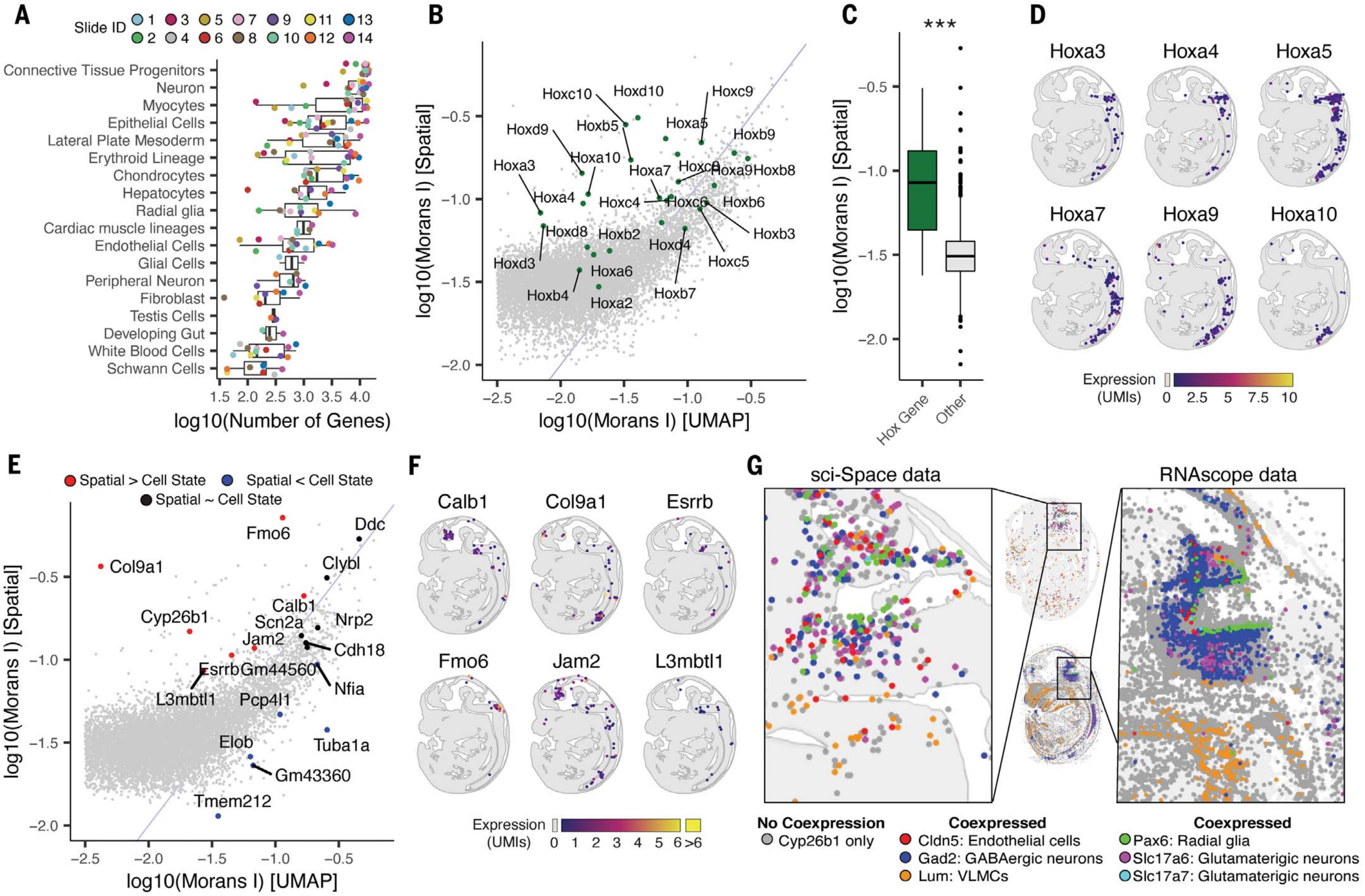

Fig. 3. Spatially restricted gene expression in developing neurons. (**A**) Number of spatially significant (Moran's test, FDR < 0.001) autocorrelated genes within each slide (color) and cell type. Only cell types with >50 cells per slide were included. (**B**) Log-log (log10) plot of autocorrelation in UMAP embedding (*x*-axis) versus autocorrelation in spatial coordinates (*y*-axis) for each gene computed on excitatory neurons from slide 1. Moran's I values close to 1 indicate perfect spatial correlation, and a value of 0 indicates a random spatial distribution. Hox genes are highlighted. (**C**) log10-scale boxplot of Moran's I statistic for Hox genes displayed in (B) versus all other expression level–matched genes ($P < 0.001$, two-sided t test). (**D**) Gene expression of HoxA cluster in slide 1. (**E**) Similar to (B), log-log (log10) plot of autocorrelation in UMAP embedding (*x*-axis) versus autocorrelation in spatial coordinates (*y*-axis) for each gene with genes in different regimes highlighted for slide 1. (**F**) Expression patterns across slide 1 for other spatially restricted genes that are not restricted to a single neuron subcluster. (**G**) Comparison of sci-Space (slide 14)– and RNA FISH (RNAscope)–detected *Cyp26b1* patterns of expression (gray) and coexpression with markers (colors as indicated in key) for neuronal and supportive cell types.

compared this value with its autocorrelation in UMAP space (UMAP Moran's I), a proxy for gene expression driven by a single-cell subtype. Across all genes, the two measures were reasonably well correlated (Pearson's rho 0.49, $P < 2 \times 10^{-16}$). However, a subset of genes, particularly in neurons, displayed higher spatial autocorrelation in the tissue context than in UMAP space (Fig. 3B and fig. S25, A and B). For example, Hox genes, a class of homeotic transcription factors that specify the body plan, featured prominently in this subset, consistent with spatial patterning that could not be explained solely by spatial restriction of a single-cell subtype (Fig. 3, B and C, and fig. S25, A to D). Expression of HoxA cluster genes paralleled the establishment of the spinal cord's anterior-posterior axis (*29*) (Fig. 3D and fig. S25), with no cell subtype restriction observed across datasets (*30*) or modalities (fig. S26, A to C).

Additional non-Hox genes also displayed excess spatial autocorrelation (Fig. 3, E and F, and fig. S26D). One such gene, *Cyp26b1*, encodes an enzyme that metabolizes the developmental morphogen retinoic acid. The spatial distribution of morphogens such as retinoic acid can play a critical role in tissue patterning (*29*). sci-Space data localized the focal expression of *Cyp26b1* to the brainstem with expression observed in multiple neuronal subclusters (figs. S25, A and B, and S26, A and B). This result was validated by RNA fluorescence in situ hybridization (FISH) for *Cyp26b1* and neuronal subtype–specific genes (Fig. 3G and fig. S26C). Together, these data identify *Cyp26b1* expression both in progenitors (radial glia) lining the hindbrain and in their progeny, spatially adjacent postmitotic neurons, suggesting that the expression of *Cyp26b1* is retained as these cells differentiate. This example illustrates how sci-Space can distinguish between spatial patterns of gene expression driven by a single-cell type from those present across multiple cell types.

Quantifying the explanatory power of spatial position

To investigate how each cell type's transcriptome varied globally across the embryo, we calculated the angular distance between the transcriptomes of pairs of cells of the same type separated by varying distances. For many cell types, as the physical distance between cells increased, so did the angular distance between their transcriptomes. However, this trend varied considerably, e.g., it was particularly pronounced

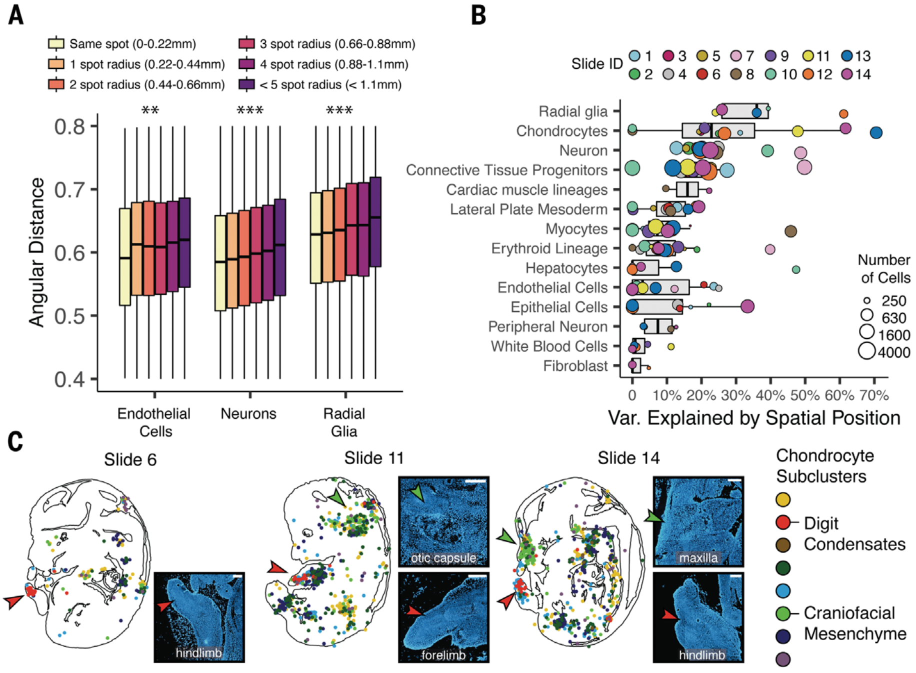

Fig. 4. Quantifying the variance in gene expression attributable to spatial position. (**A**) Pairwise angular distance (radians) between global transcriptomes of cells of the indicated cell types. Cell pairs are grouped by distance on the physical array (millimeters) ($^{**}P < 0.001$, $^{***}P < 0.0001$, Wald linear regression test). (**B**) Proportion of nontechnical variance explained within cells of each type by spatial position. Point size indicates number of cells and point color indicates the slide of origin. (**C**) Recovered positions of chondrocytes from slides 6, 11, and 14 colored by subcluster. Arrows indicate focal concentrations of craniofacial mesenchyme (green) and digit condensate subclusters (red). Insets to the right of each plot show parts of each image with similarly positioned arrows. White text of each inset labels the anatomic structure displayed. Scale bars in (C), 0.25 mm.

in radial glia, neurons, and endothelial cells (Fig. 4A and fig. S27, A and B).

To quantify the contribution of spatial context to variation in gene expression across individual cells, we developed a statistical approach. Briefly, we first partitioned cells into groups on the basis of cell type and spatial location. Then, we computed the angular distance between each cell and the average expression profile for cells of that same type in the same spatial bin. After estimating and subtracting the technical variance attributable to data sparsity, we quantified how much of the remaining biological variance was due to each cell's type and/or spatial position. To validate this approach, we decomposed the variance attributed to lineage in the developing *Caenorhabditis elegans* embryo, where there is a relationship between two cells' lineage relationship and their observed gene expression variance (*2*). We found that our variance decomposition approach followed the law of total variance (fig. S28C) and, in agreement with Packer *et al.* (*2*), showed that variance attributable to a cell's lineage relationship peaked around generation 7 (fig. S28D).

Applying this variance decomposition approach to the sci-Space data, we estimated that sparse UMI sampling accounted for 95.1% of the observed variance in global gene expression across cells and in subsequent analyses, we focused on the remaining 4.9% "nonsampling" variance. Of this nonsampling variance in global gene expression, cell type alone accounted for 19%. However, a joint model that included both cell type and spatial position accounted for 50% (fig. S29). The implication, that spatial information explains as much, if not more, of nonsampling gene expression variance as major cell type, was supported by the recovery of cell type and spatial gene modules of similar size and composition (fig. S30). However, some cell types' transcriptomes appeared more sensitive to spatial position than others (Fig. 4B). For example, chondrocytes were influenced by position within the embryo, reflecting the ongoing development of various connective tissue lineages at E14.0, and explained at least in part by subclusters that appear to correspond to digit condensates and craniofacial mesenchyme (Fig. 4C and fig. S31). Other such cell types included neurons and their precursors, the radial glia.

Pseudotemporal sci-Space trajectories reflect neuronal migration dynamics

To explore how spatial context might relate to gene expression heterogeneity in a developing cell lineage, we focused on radial glia and neurons. In particular, we hypothesized that we might be able to detect and localize the coordinated processes of neuronal differentiation and migration (*31*). UMAP dimensionality reduction of these cell types revealed the presence of three distinct trajectories originating in radial glia and leading to neurons (Fig. 5A). Gene expression dynamics along these three branches were consistent with neuronal differentiation, the up-regulation of cell cycle genes followed by expression of genes involved in migration (fig. S32). Each branch was strongly enriched for subtype-specific marker gene expression, Pou4f1$^+$/Pax3$^+$ tectal neurons, Isl1$^+$/Lhx6$^+$ cortical interneurons, and Emx1$^+$/Neurod6$^+$ cortical pyramidal neurons, indicating that the embedding captures their specification from radial glia (Fig. 5B). We examined how these trajectories were anatomically distributed by segmenting the brain from each section using the Allen Institute's Anatomical Reference Brain Atlas (http://atlas.brain-map.org/) as a guide. Cells from each trajectory overwhelmingly occupied a distinct brain region (Fig. 5C). To quantify progression through differentiation, we calculated pseudotime for each branch using radial glia as the root (Fig. 5D and fig. S32). Intersecting pseudotime and spatial information, we observed that cells early in differentiation clustered around the ventricles in the forebrain and developing midbrain, whereas those farther away exhibited a more differentiated transcriptome (Fig. 5E and fig. S33).

The spatial gradients of cellular maturity estimated with sci-Space data are consistent with well-documented coordination of cellular differentiation and neuronal migration. In the pallium, immature neurons migrate and differentiate radially outward, leading to the inside-out development of the cortical layers (*31*). In the subpallium, cortical interneurons born in the ganglionic eminences migrate tangentially to populate the developing cortex and olfactory bulb (*32*). Our data also identify a third major pattern of migration in which precursors emanate from the dorsal aspect of the ventricular zone in the developing midbrain. These midbrain neurons seem to migrate both radially, toward the pial surface, and tangentially, parallel to the pial surface, to populate this region (Fig. 5E, slides 8, 13, and 14, and fig. S33, slides 4 and 7). Although radial and tangential migration are generally discussed as being mutually exclusive phenomena, our data, consistent with some prior work (*33*, *34*),

Fig. 5. Pseudotemporal spatial trajectories capture migratory patterns in the developing brain. (**A** to **D**) UMAP embedding displaying the neural trajectories colored by cell type (A), specific gene expression (B), cortical region (C), or pseudotime (D). (**E**) Neurons and radial glia in the cortex are colored by pseudotime or are otherwise colored gray. Insets of caudal (top) and rostral (bottom) brain outlines are shown to the right of each slide. M, midbrain; P, pallium; SP, subpallium; V, ventricle). (**F**) Scaled and centered gene expression for genes (rows) significantly varying over pseudotime in all three trajectories. Enriched Gene Ontology Biological Processes terms (GO BP) are displayed next to clustered genes.

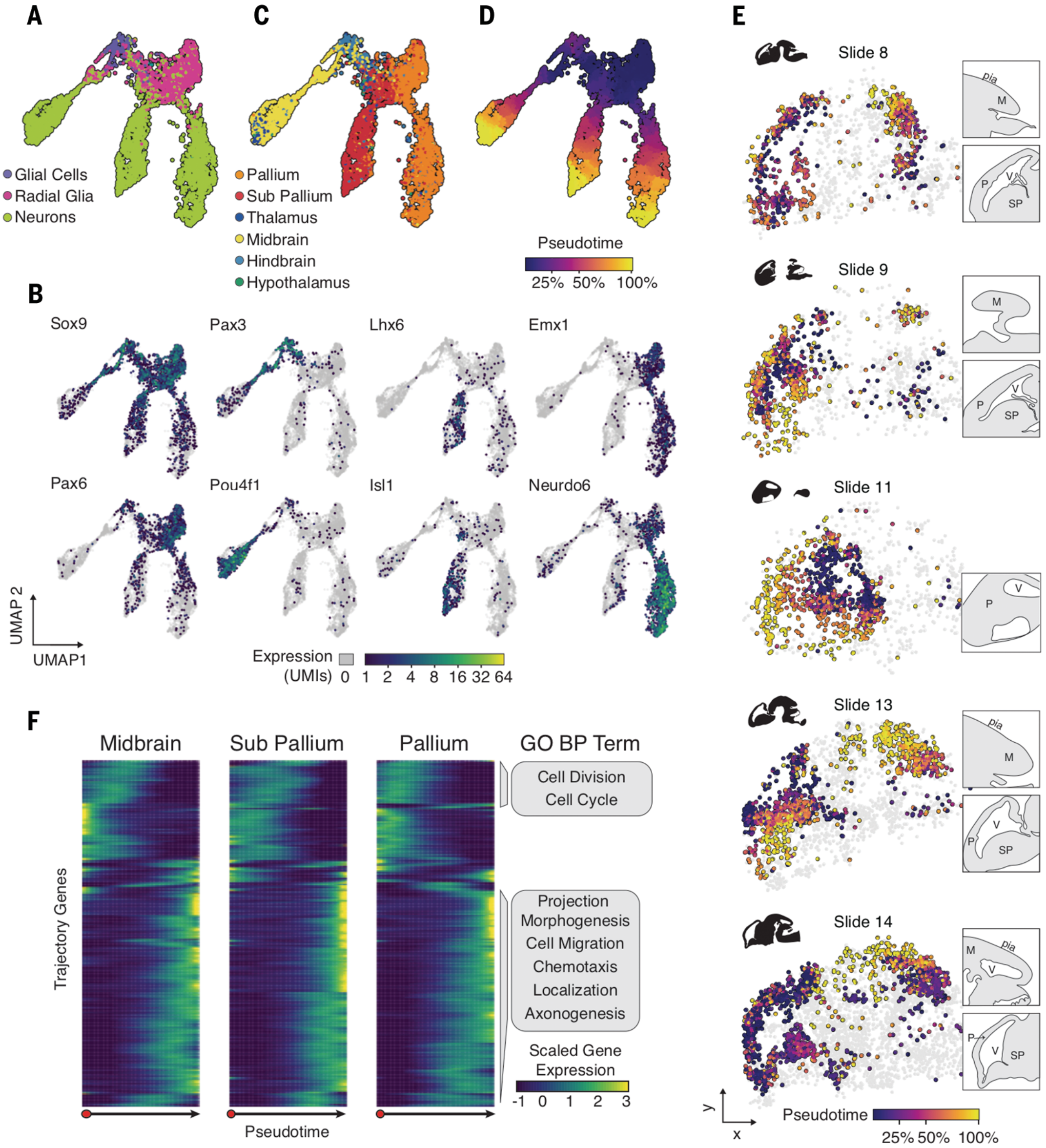

suggest otherwise in the developing midbrain. Furthermore, these cells share a common transcriptional program with differentiating and migrating neurons in the pallium and subpallium (Fig. 5F and data file S3).

Discussion

sci-Space is a method for spatial transcriptomics that retains single-cell resolution while capturing spatial information at a scale specified by a patterned array of cell hashing oligos. As a proof of concept, we applied sci-Space to retrieve the approximate spatial coordinates of transcriptionally profiled cells across whole-mount sections from E14.0 mouse embryos. The sci-Space data are readily integrated with nonspatial single-cell RNA-seq data collected from mouse embryos at adjacent time points (*1*, *21*), enabling rapid annotation of diverse cell types and visualization of cell-type–specific, spatially patterned gene expression, i.e., digital in situs. We identify examples, some expected and others unexpected, of genes expressed in an anatomically patterned manner within cells of a given type.

The spatial resolution of sci-Space is presently limited by the patterned array of hashing oligos, here to ~200 μm. Although increasing spot density and decreasing spot size are a straightforward path to increasing resolution, sci-Space is unlikely to detect effects arising from interactions between adjacent cells. This is limited by recovery of only a fraction of cells from each serial section such that we obtain a "survey" rather than achieving dense measurements. Nonetheless, sci-Space fills a need not addressed by other technologies. Like other STC methods (e.g., Slide-seq), sci-Space can be applied routinely and efficiently to large regions, e.g., whole-embryo serial sections. However, unlike these methods, sci-Space recovers single-cell transcriptomes. It can therefore capture patterns of spatial gene regulation private to specific cell types and estimate the contribution of each cell type to the expression of morphogens and other signaling molecules, both within and across anatomical regions. Moreover, sci-Space data can serve as a spatial "scaffold" for conventional, nonspatial single-cell RNA-seq atlases, which may be more challenging to map onto tissues profiled by spatial profiling methods that lack single-cell resolution.

Finally, using these spatially resolved single-cell data, we developed a statistical approach to identify cell types in the developing embryo that exhibit spatially regulated gene expression. Closer analysis of radial glia and neurons revealed gradients of developmental maturity in different regions of the brain indicative of known and new patterns of neuronal migration. Together with data from complementary technologies, we anticipate that the further application of sci-Space to serial sections spanning entire embryos from many time points will facilitate the construction of a set of highly time- and space-resolved four-dimensional atlases of gene expression across mammalian development.

REFERENCES AND NOTES

1. J. Cao *et al.*, *Nature* **566**, 496–502 (2019).
2. J. S. Packer *et al.*, *Science* **365**, eaax1971 (2019).
3. J. A. Briggs *et al.*, *Science* **360**, eaar5780 (2018).
4. B. Pijuan-Sala *et al.*, *Nature* **566**, 490–495 (2019).
5. J. A. Farrell *et al.*, *Science* **360**, eaar3131 (2018).
6. N. Karaiskos *et al.*, *Science* **358**, 194–199 (2017).
7. D. A. Cusanovich *et al.*, *Nature* **555**, 538–542 (2018).
8. P. P. L. Tam, J. W. K. Ho, *Development* **147**, dev179788 (2020).
9. X. Qiu *et al.*, *Nat. Methods* **14**, 979–982 (2017).
10. J. Liao, X. Lu, X. Shao, L. Zhu, X. Fan, *Trends Biotechnol.* **39**, 43–58 (2021).
11. P. L. Ståhl *et al.*, *Science* **353**, 78–82 (2016).
12. S. G. Rodriques *et al.*, *Science* **363**, 1463–1467 (2019).
13. K. H. Chen, A. N. Boettiger, J. R. Moffitt, S. Wang, X. Zhuang, *Science* **348**, aaa6090 (2015).
14. S. Shah, E. Lubeck, W. Zhou, L. Cai, *Neuron* **92**, 342–357 (2016).
15. J. H. Lee *et al.*, *Science* **343**, 1360–1363 (2014).
16. S. R. Srivatsan *et al.*, *Science* **367**, 45–51 (2020).
17. M. C. Regier *et al.*, *Lab Chip* **19**, 2114–2126 (2019).
18. S. L. Wolock, R. Lopez, A. M. Klein, *Cell Syst.* **8**, 281–291.e9 (2019).
19. L. Haghverdi, A. T. L. Lun, M. D. Morgan, J. C. Marioni, *Nat. Biotechnol.* **36**, 421–427 (2018).
20. T. Stuart *et al.*, *Cell* **177**, 1888–1902.e21 (2019).
21. G. La Manno, bioRxiv 184051 [Preprint]. 3 July 2020. https://doi.org/10.1101/2020.07.02.184051.
22. H. A. Pliner, J. Shendure, C. Trapnell, *Nat. Methods* **16**, 983–986 (2019).
23. T. Pietzsch, S. Saalfeld, S. Preibisch, P. Tomancak, *Nat. Methods* **12**, 481–483 (2015).
24. J. Schindelin *et al.*, *Nat. Methods* **9**, 676–682 (2012).
25. P. Thévenaz, U. E. Ruttimann, M. Unser, *IEEE Trans. Image Process.* **7**, 27–41 (1998).
26. R. Dries *et al.*, bioRxiv 701680 [Preprint]. 13 July 2019. https://doi.org/10.1101/701680.
27. G. Diez-Roux *et al.*, *PLOS Biol.* **9**, e1000582 (2011).
28. D. Fawkner-Corbett *et al.*, *Cell* **184**, 810–826.e23 (2021).
29. A. Sagner, J. Briscoe, *Development* **146**, dev182154 (2019).
30. J. Delile *et al.*, *Development* **146**, dev.173807 (2019).
31. B. Nadarajah, J. E. Brunstrom, J. Grutzendler, R. O. Wong, A. L. Pearlman, *Nat. Neurosci.* **4**, 143–150 (2001).
32. M. Turrero García, C. C. Harwell, *FEBS Lett.* **591**, 3942–3959 (2017).
33. S.-S. Tan, H. Valcanis, M. Kalloniatis, A. Harvey, *Dev. Biol.* **241**, 117–131 (2002).
34. Y. Watanabe, C. Sakuma, H. Yaginuma, *Dev. Biol.* **437**, 131–139 (2018).
35. S. R. Srivatsan, M. Regier, Cole-trapnell-lab/sci-Space: Initial release, Zenodo (2021); https://doi.org/10.5281/ZENODO.4698159.
36. S. Srivatsan, M. Regier, Creating sci-space grids for spatial barcoding v1 (protocols.Io.Bm64k9gw), Protocols.io (2020); https://doi.org/10.17504/protocols.io.bm64k9gw.
37. S. Srivatsan, M. Regier, Spatial transfer of oligonucleotides and imaging v2 (protocols.Io.Btw5npg6), Protocols.io (2021); https://doi.org/10.17504/protocols.io.btw5npg6.
38. S. Srivatsan, J. Cao, Single cell RNA sequencing library preparation v1 (2-level sci-RNA-seq) (protocols.io.bquamwse), Protocols.io (2020); https://doi.org/10.17504/protocols.io.bquamwse.

ACKNOWLEDGMENTS

We thank members of the Lampe, Stevens, Shendure, and Trapnell laboratories for critical discussions and feedback, particularly V. M. Rachleff, E. Nichols, R. Daza, J. Cao, V. Ramani, and L. Saunders. **Funding:** Aspects of this work were supported by the NIH (1U54HL145611 to C.T. and J.S.; UM1HG011586 to C.T. and J.S.; 1R01HG010632 to C.T. and J.S.; DP2HL137188 to K.R.S.; and T32EB1650 to S.S.), the Deutsche Forschungsgemeinschaft (SP1532/3-1;4-1;5-1 to M.S), the Brotman Baty Institute for Precision Medicine, the Paul G. Allen Frontiers Foundation (Allen Discovery Center grant to J.S. and C.T.), and the Washington Research Foundation (postdoctoral fellowship to M.C.R.). J.S. is an investigator of the Howard Hughes Medical Institute. **Author contributions:** S.R.S. and M.C.R. conceptualized and performed the experiments. J.L. aided in sci-Space slide fabrication with support from P.L. S.R.S. and M.C.R. performed the computational analyses with assistance from E.B., P.G., J.F., M.D., and J.P. and under the supervision of C.T. M.S. and C.L. provided critical feedback on the project. S.R.S., M.C.R., C.T., K.R.S., and J.S. wrote the manuscript with input from all authors. K.R.S., J.S., and C.T. supervised the project. **Competing interests:** One or more embodiments of one or more patents and patent applications filed by the University of Washington may encompass the methods, reagents, and data disclosed in this manuscript. **Data and materials availability:** Processed and raw data can be downloaded from the National Center for Biotechnology Information (NCBI) under GSE166692. Code used to reproduce the presented analyses is indexed on Zenodo (*35*). Laboratory protocols can be found on protocols.io (*36*–*38*).

SUPPLEMENTARY MATERIALS

science.sciencemag.org/content/373/6550/111/suppl/DC1
Materials and Methods
Figs. S1 to S33
Tables S1 and S2
References (*39*–*42*)
Data Files S1 to S3
MDAR Reproducibility Checklist

View/request a protocol for this paper from *Bio-protocol*.

30 March 2020; resubmitted 13 February 2021
Accepted 24 May 2021
10.1126/science.abb9536